How incoming turbulence affects wake recovery of an NREL-5MW wind turbine

Stefania Cherubini, Giovanni De Cillis, Onofrio Semeraro, Stefano Leonardi, Pietro De Palma

Journal of Physics: Conference Series

PAPER • OPEN ACCESS

How incoming turbulence affects wake recovery of an NREL-5MW wind turbine

To cite this article: Stefania Cherubini *et al* 2022 *J. Phys.: Conf. Ser.* **2385** 012139

How incoming turbulence affects wake recovery of an NREL-5MW wind turbine

Stefania Cherubini[1], Giovanni De Cillis[4], Onofrio Semeraro [3], Stefano Leonardi [2], Pietro De Palma [1]

[1]Dipartimento di Meccanica, Matematica e Management, Politecnico di Bari, Via Re David 200, Bari, Italy
[2]Department of Mechanical Engineering, University of Texas, Dallas, Texas, USA
[3]LISN, Université de Paris-Saclay, CNRS, Orsay, France
[4] CMCC, Via Marco Biagi 5, Lecce, Italy

E-mail: stefania.cherubini@poliba.it

Abstract. The present work aims at investigating the effect of inflow turbulence on the wake recovery of the NREL-5MW reference wind turbine. The wake produced by a utility-scale wind turbine invested by both a laminar uniform inflow and a turbulent flow, is analyzed by means of proper-orthogonal decomposition (POD). The considered turbine is the NREL-5MW at tip-speed ratio $\lambda = 7$ and a diameter-based Reynolds number of the order 10^8. The flow is simulated through Large Eddy Simulation, where the forces exerted by the blades are modeled using the Actuator Line Method, whereas tower and nacelle are modeled employing the immersed boundary method. The main flow structures identified by modal decomposition in both of the considered cases are compared, and some differences emerge, which can be of great importance for the formulation of a reduced-order model. Among the most energetic modes, a high-frequency mode directly related to the tip vortices is found only in the flow case with laminar inflow. In the presence of inflow turbulence, the most energetic modes are all composed by large-scale low-frequency structures filling the whole domain. We evaluate the contribution of each POD mode to wake recovery reconstructing the total flux of mean kinetic energy due to turbulent fluctuations on a closed surface enclosing the wake of the wind turbine. In the laminar-inflow case, we have found that the POD modes related to the tip and root vortices do not contribute positively to the wake recovery, but they rather sustains the velocity gradient, as already established by Lignarolo et al. (2015) for a wind-turbine model. Whereas, in the turbulent-inflow case, all the most energetic modes contribute positively to wake recovery. These results clearly indicate that inflow turbulence should be taken into account for accurately estimate the entrainment process in the wake of wind turbines.

NREL 5MW wind turbine, POD, laminar or turbulent inflow, wake recovery, turbulent kinetic energy entrainment

1. Introduction

According to the current National Energy and Climate Plans 2021-2030 [1] and after the approval of the recent RepowerEU program, the European Union aims at cutting the greenhouse gas emissions by at least 45% in comparison with 1990 levels. Due to this urgent need to reduce greenhouse-gas emissions and the dependence upon fossil fuels, a significant increase in the energy demand from renewable sources took place in the last decades, so much so that, in 2018,

the renewable power-capacity reached 33% of the total one [2]. Among others, technologies for the exploitation of the wind resource are one of the most reliable and with a long history of commercial success. Wind energy contributes to 25% of the global renewable power-capacity, and it is the first renewable source after the hydropower [2]. The global wind-power market expanded of 19% in 2019 thanks to an increase of 60 GW in the power capacity [3]. However, the needed acceleration in the deployment of wind power installations for reaching the Paris goals will require still more investment in new technologies and/or optimization of the existing ones [4].

Wind turbines are usually clustered into farms, where they become aerodynamically coupled to each-other through the presence of their wakes [5, 6]. In fact, when placed in the wake of an upstream one, a turbine will produce considerably less power, depending on the relative position of the turbines. The resulting reduction of power production may reach 40% in plants having a high power density (i.e., a reduced distance among the turbines). This issue motivates researchers to look for innovative ways of optimizing the farm efficiency while keeping high the power density. Among other possible solutions, one can control the axial induction [7, 8] or the wake direction [9, 10] of the turbines. However, these promising methods rely on large-eddy simulation (LES) of large wind farms, which have a huge computational cost.

This drawback is leading to an increased interest towards the development of low-dimensional models of the wake dynamics. These reduced-order models can be fed into simulations of the downwind turbines, allowing a much computationally cheaper estimate of their power production and consequently optimize their relative placement.

Low-dimensional models of the wake are usually developed using modal decomposition applied to numerical or experimental data. One notable example is the proper orthogonal decomposition (POD) (see Ref.s [11, 12]), although other techniques such as the Dynamic Mode Decomposition are becoming popular as well [13]. In Ref. [14], POD is applied to the numerical study of a wind farm, finding that streamwise counter-rotating rolls play a crucial role in the kinetic-energy redistribution and thus have a considerable impact on wind-farm efficiency. In Ref. [15], wake recovery is investigated using POD applied to velocity measurements of turbine arrays, effectively reproducing the turbulence kinetic energy production and flux of turbulence kinetic energy using $\approx 1\%$ of the total orthogonal modes. More recently, in Ref.s [16] and [17], POD has been used to investigate the effect of the presence of tower and nacelle on the development of coherent structures within the wake, evaluating the contribution of each POD mode to wake recovery. They found that tip vortices have a negative contribution to the entrainment of turbulent kinetic energy within the wake, and thus hinder wake recovery. This result is in agreement with the quadrant analyses in Ref. [18], showing that tip vortices do not provide any contributions to the overall turbulent mixing, and with the observations in Ref. [19], reporting even a shielding effect of the tip vortices, which prevent the near-wake shear layer to recover.

However, many of these studies consider a uniform laminar inlet flow impacting the wind turbine. This is an ideal condition, rarely encountered in real applications, where wind turbines operate in the atmospheric boundary layer (ABL), the features of which are determined by several factors like thermal stratification, topography etc. The ABL characteristics (turbulence intensity, mean velocity profile, etc.) certainly affect the turbine power production and the wake dynamics, as recently assessed in Ref.s [20, 21, 22, 23]. It is now well known that an increase of the turbulence intensity of the flow impinging on the turbine correlates well with a faster wake recovery [24, 25, 26]. This is due to the fact that the diffusion provided by the turbulent fluctuations enhances the transport of mean kinetic energy within the wake. However, is it not yet clear how the coherent structures created by the interaction of the turbulent ABL and the wake, impact on the entrainment mechanism which leads to wake recovery.

For laminar inflow conditions, the near-wake is characterized by very energetic vortical structures shed from the tip and the root of the rotor blade, i.e., the tip- and root-vortices, which become

unstable breaking down towards small-scale turbulent structures. The turbulent fluctuations generated by the breakdown of these coherent vortices and by the entrainment of the outer flow, eventually lead to wake recovery [27, 28]. However, as recently shown in Ref. [23] by means of dynamic mode decomposition, these highly energetic vortical structures loose their dynamical relevance when the turbine is impinged by a turbulent inflow. This suggests that the entrainment of the outer flow as well as the wake recovery, might be considerably affected as well.

This work aims at establishing the impact of athmospheric turbulence on the coherent structures characterizing the wake, and how these affect the entrainment mechanism towards wake recovery. This is accomplished by determining, by means of POD analysis, the most energetic coherent structures shed by the turbine in the presence and in the absence of inflow turbulence, and using them to reconstruct the total flux of mean kinetic energy due to turbulent fluctuations on a closed surface enclosing the wake of the wind turbine. This analysis will show that the impact of inflow turbulence on the process of turbulent kinetic energy entrainment and wake recovery is remarkable, indicating that inflow turbulence should be taken into account for accurately estimate the entrainment process in the wake of wind turbines.

The paper is structured as follows. Section 2 presents the numerical methods used for the present investigation, ranging from LES to POD. Then, in section 3, the simulation setup is defined. Results about POD of the flow in the wake of the considered turbine are presented in section 4, whereas the mean kinetic energy entrainment is evaluated in section 5. Relevant conlusions are provided in section 6.

2. Methodology

The dataset used for studying the wake recovery of the flow past an NREL-5MW wind turbine in the presence or in the absence of inflow turbulence, in constituted by snaphots extracted from Large-Eddy-Simulations of the flow field. Using an in-house numerical code, the following filtered Navier-Stokes equations are integrated in time

$$\frac{\partial u_i}{\partial t} + \frac{\partial u_i u_j}{\partial x_j} = -\frac{\partial p}{\partial x_i} + \frac{1}{Re}\frac{\partial^2 u_i}{\partial x_j \partial x_j} - \frac{\partial \tau_{ij}}{\partial x_j} + F_i, \tag{1}$$

$$\frac{\partial u_i}{\partial x_i} = 0, \tag{2}$$

where $\boldsymbol{u}$ is the filtered non-dimensional velocity, p the pressure, τ_{ij} is the (modeled) subgrid-scale stress tensor, F_i is a forcing term, the subscripts $i, j \in \{1, 2, 3\}$ indicate the streamwise, x, vertical, y, and transverse, z, directions, respectively, and $Re = U_\infty D/\nu$ is the Reynolds number based on the inlet velocity U_∞, the rotor diameter D and the kinematic viscosity of the fluid ν. For modeling the effect of the small-scale structures on the filtered flow, a Smagorinsky model with constant $C_S = 0.17$ is used, which is close to the theoretical value typically used for LES. The governing equations are discretised in space using second-order centered finite-differences on a staggered Cartesian grid. A hybrid low-storage third-order-accurate Runge-Kutta scheme is adopted for integrating the equations in time [29].

The aerodynamic forces (per unit volume) exerted by the turbine blades on the fluid are simulated by using the actuator line method [30], which is based on the use of a forcing term (F_i in equation (1)) whose value is determined by the lift and drag coefficients of the rotor blades. Each blade is treated as a rotating rigid line divided into discrete segments whose lift and drag forces (per unit length) are estimated given the angle of attack and the relative inflow velocity. These forces are spread on areas perpendicular to each segment using a Gaussian distribution kernel. Concerning the tower and nacelle, these are simulated by using the immersed boundary method [31], which is a rather computationally cheap method with respect to those using body-fitted grids.

2.1. Proper Orthogonal Decomposition

Proper Orthogonal Decomposition (POD) is a useful tool for analysing experimental or numerical datasets from a statistical point of view, since it provides an energetically optimal orthogonal basis for decomposing the data. In the case under consideration, it provides the most energetic coherent structures characterising the flow field $\mathbf{q}(\mathbf{x}, t)$ [32].

The method is based on evaluation of the two-point spatial correlation tensor $\mathbf{C}$, whose eigenvectors are the POD modes, having energy provided by the associated eigenvalues. The tensor $\mathbf{C}$ can be approximated based on a large number M of equally-spaced snapshots of the flow field. These snapshots are organised into a single matrix $\mathbf{Q} \in \mathbb{R}^{N \times M}$, whose columns are the M instantaneous velocity fields of dimension N, which is then employed as follows:

$$\mathbf{C} = \frac{1}{M}\mathbf{Q}\mathbf{Q}^T, \tag{3}$$

to provide the two-point spatial correlation tensor $\mathbf{C} \in \mathbb{R}^{N \times N}$. The eigenvalues/eigenvectors of $\mathbf{C}$ are then recovered using singular value decomposition of the snapshot matrix $\mathbf{Q}$, divided by the square root of the number of snapshots M,

$$\frac{\mathbf{Q}}{\sqrt{M}} = \mathbf{U}\mathbf{S}\mathbf{V}^T, \tag{4}$$

where the left singular vector $\mathbf{U}$ has size $N \times M$, each column $\boldsymbol{\phi}_k$ corresponding to a POD mode, and the singular values squared correspond to the eigenvalues of $\mathbf{C}$. The stochastic process $\mathbf{q}(\mathbf{x}, t)$ can be thus reconstructed by a linear combination of the mutually-orthogonal POD modes:

$$\mathbf{q}(\mathbf{x}, t) = \sum_{k=1}^{M} a_k(t)\boldsymbol{\phi}_k(\mathbf{x}) \tag{5}$$

where the time coefficients of each POD mode, a_k, given by the rows of the matrix $\sqrt{M}\mathbf{S}\mathbf{V}^T$, represent the inner product between the POD modes and the snapshots, as $a_k(t) = \langle \boldsymbol{q}(\boldsymbol{x}, t), \boldsymbol{\phi}_k(\boldsymbol{x}) \rangle$. Notice that the spatial modes $\boldsymbol{\phi}(\boldsymbol{x})$ are chosen so as to maximize the quantity:

$$\sigma = \frac{E\{|\langle \boldsymbol{q}(\boldsymbol{x}, t), \boldsymbol{\phi}(\boldsymbol{x}) \rangle|^2\}}{\langle \boldsymbol{\phi}(\boldsymbol{x}), \boldsymbol{\phi}(\boldsymbol{x}) \rangle}, \tag{6}$$

where $E\{\cdot\}$ is the expectation operator, which in the case of space-only POD, corresponds to a time-average and $\langle \cdot, \cdot \rangle$ is the inner product associated with the Hilbert space to which the stochastic process belongs.

3. Simulation setup

An NREL-5MW wind turbine, having diameter $D = 126\,\mathrm{m}$ and hub-heigth $h = 87.5\,\mathrm{m}$, is simulated at rated conditions with tip-speed ratio $\lambda = 7$, with a constant dimensionless angular frequency of the rotor $\omega = 2\lambda = 14$ and a reference incoming wind speed $U_\infty = 11.4\,\mathrm{m/s}$. The diameter-based Reynolds number is about equal to 10^8.

A computational domain of size $12.5 \times 5 \times 3$ diameter units in the x,y,z directions is considered, where the turbine is placed at 4 diameter units from the inlet, centered in the transverse direction. No-slip and free-slip conditions are imposed at the lower and upper boundaries, respectively. Periodicity is imposed in the transverse direction. At the outlet boundary, a radiative condition is employed, having uniform convection velocity $c = 0.9$ [33]. Concerning the inlet conditions, two cases are considered: a laminar-inflow case in which a uniform velocity U_∞ is imposed, and a turbulent-inflow case in which a flow mimicking a turbulent athmospheric boundary layer is imposed.

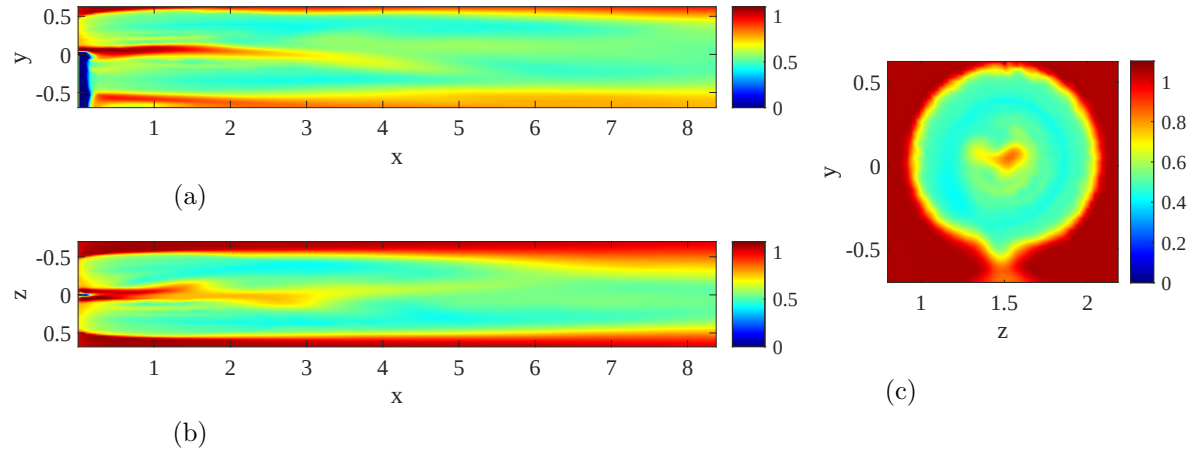

Figure 1: Streamwise velocity contours of the snapshots' ensemble mean for the laminar inflow case. (a) $x-y$ plane at $z=1.5$. (b) $x-z$ plane at $y=0$. (c) $z-y$ plane at $x=4$.

The computational grid is composed of $2048\times512\times512$ grid-points in x, y, z, respectively. The points are equally spaced along the streamwise and transverse directions and are stretched in the vertical direction. A grid-convergence study of the LES results is provided in Ref. [17].
In order to obtain the inlet boundary condition for the turbulent-inflow case, we perform a precursor simulation at the same value of the Reynolds number employed in the laminar-inflow case. The computational domain for the precursor simulation has dimensions $6\times5\times3$ diameter units in the x,y,z directions, respectively. No-slip is imposed at the bottom wall, whereas, at the upper boundary, vertical velocity and shear are set to zero. In x and z directions, periodicity is imposed. For triggering turbulence, we place at the wall a staggered array of cubes of height $h_c=0.1$ [34] mimicking wall roughness. As shown in detail in Ref. [23], the time- and space-averaged streamwise velocity profiles are well fitted with a logarithmic law in the inner region, starting from the region on top of the roughness elements, while the profile in the outer region is well described by a power law having shear coefficient $\alpha=0.27$. The turbulence intensity is approximately 10% at the hub height. The time-varying turbulent velocity obtained by the precursor simulation is imposed at the inlet of the computational domain for the wind turbine. Notice that, due to turbulence decay, the turbulence intensity impinging the turbine is lower than 10% at hub height.

4. Modal decomposition of the wake

POD is performed on two distinct datasets, one for the laminar- and one for the turbulent-inflow case. These datasets are composed each one by 3052 three-dimensional snapshots of the velocity field, taken each 10° rotation of rotor. POD is carried out in a subdomain of extent $[4\ \ 12.4]\times[-0.7\ \ 0.63]\times[0.8\ \ 2.2]$ in the streamwise, vertical and transverse directions, respectively. The ensemble average of the snapshots is then subtracted from each snapshot of the two datasets. The mean flow is shown in Figure 1 and 2 for the laminar- and the turbulent-inflow cases, respectively, showing relevant differences. In the former case, the velocity deficit region downstream of the turbine appears more elongated in the streamwise direction (see frames (a) and (b) of both figures), while in the latter, more diffusion of the flow can be observed (frame (c)). In particular, evaluating the wake as the region in which $U\leq0.4U_\infty$, we measure that in the turbulent-inflow case the wake length is reduced from 8 to 5 diameter units.

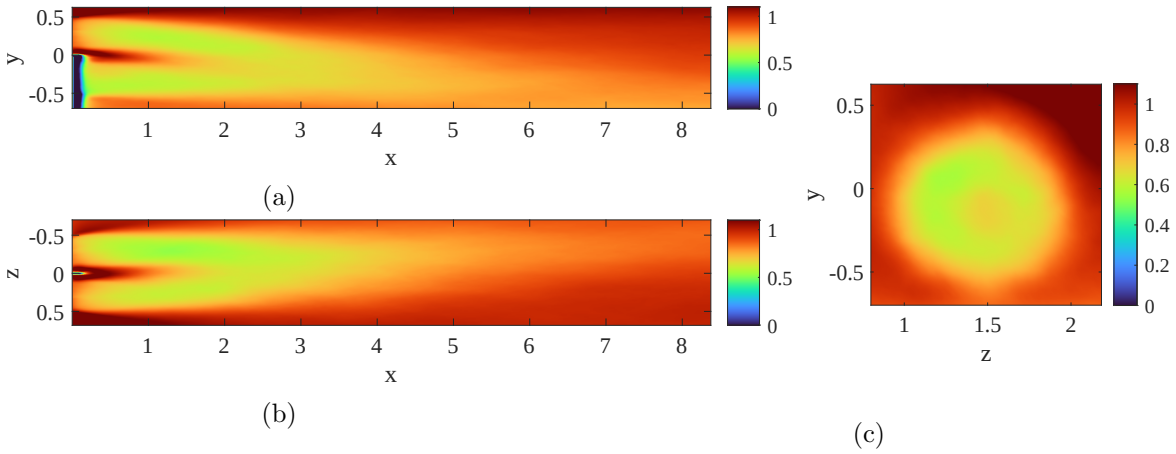

Figure 2: Streamwise velocity contours of the snapshots' ensemble mean for the turbulent inflow case. (a) $x-y$ plane at $z = 1.5$. (b) $x-z$ plane at $y = 0$. (c) $z-y$ plane at $x = 4$.

4.1. POD results

Figure 3(a) provides the distribution of the singular values for the most energetic 150 POD modes of both datasets. In both cases, a steep energy decay is observed for the first ≈ 10 modes. The slope continues decreasing more mildly towards the first ≈ 100 modes. Then, an approximately null energy is reached for $k \approx 2500$ (not shown). One can also notice that, in the turbulent-inflow case, a much larger amount of energy is contained in the first modes. The cumulative percentage distribution of turbulent kinetic energy is computed as:

$$\overline{k}[\%] = \frac{\sum_{k=1}^{m} s_k}{\sum_{k=1}^{M} s_k} \times 100 \quad m \in \{1, \ldots, M\} \tag{7}$$

$$\text{modes}[\%] = \frac{m}{M} \times 100. \tag{8}$$

This quantity is plotted in Figure 3(b) versus the percentage of POD modes taken into account in the analysis, for the laminar- (red) and the turbulent-inflow (blue) cases. In both cases, 80% percent of the turbulent kinetic energy is achieved with 40% of POD modes (~ 1200 modes). In the laminar-inflow case a fraction of modes $< 40\%$ accounts for a lower percentage of the turbulent kinetic energy than in the turbulent-inflow case. This is probably due to the fact that in the latter case the first modes bear a much larger amount of energy than in the former, suggesting that a low-order reconstruction of the flow field might be more effective in the (more realistic) turbulent-inflow case. However, for a percentage of modes $> 40\%$, this trend is reversed, since a (slightly) larger turbulent kinetic energy is reached in the laminar case for an equivalent number of modes considered.

The most energetic POD modes are shown in figure 4 (laminar-inflow case) and 5 (turbulent-inflow case). Since the most energetic modes are paired, only the odd modes will be discussed in the following. In the laminar-inflow case, the second pair, provided in figure 4(b) is characterized by small-scale structures placed very close to the turbine, and clearly corresponds to the tip vortices. Whereas, all the other (most energetic) modes are mostly localized in the far wake and characterized by coherent motions of rather larger length scale (of the order of the turbine's diameter at most). As discussed in Ref. [17], these intermediate-scale structures are generated by the interaction of the vortices shed by the tower and nacelle with the shear generated by the rotor. Very interestingly, the most energetic coherent structures for the turbulent-inflow case are remarkably different, as shown in figure 5. They are all characterized by elongated flow

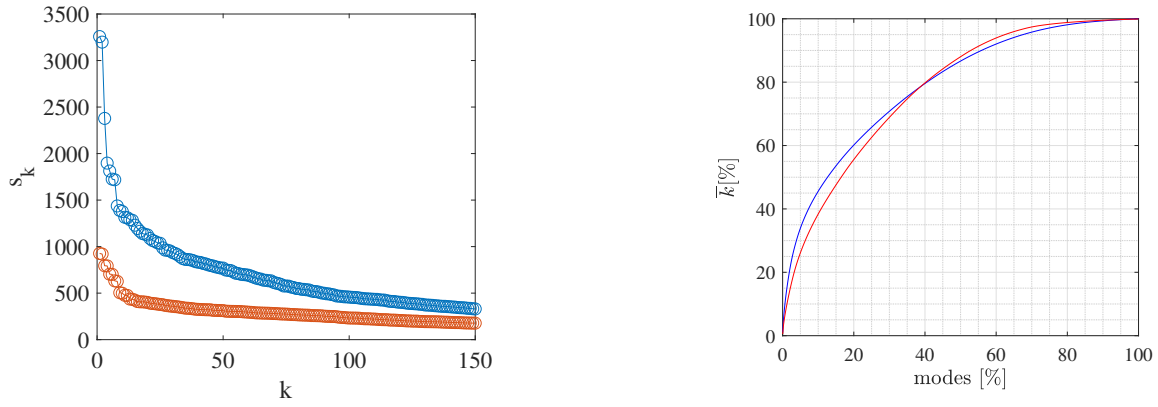

(a) (b)

Figure 3: (a) Singular values distribution of the first 150 POD modes and (b) cumulative turbulent kinetic energy distribution versus the fraction of POD modes for the laminar (red) and the turbulent (blue) inflow cases.

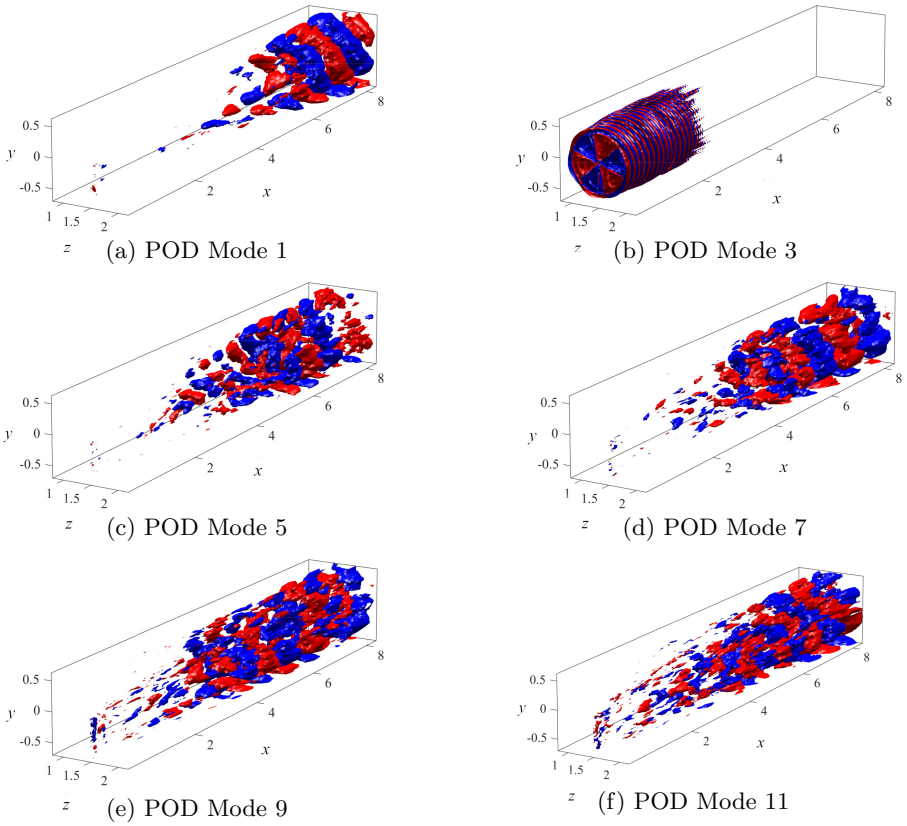

(a) POD Mode 1 (b) POD Mode 3

(c) POD Mode 5 (d) POD Mode 7

(e) POD Mode 9 (f) POD Mode 11

Figure 4: Streamwise velocity iso-surfaces of the most energetic POD modes (red for $u = 0.001$, blue for $u = -0.001$) for the laminar-inflow case.

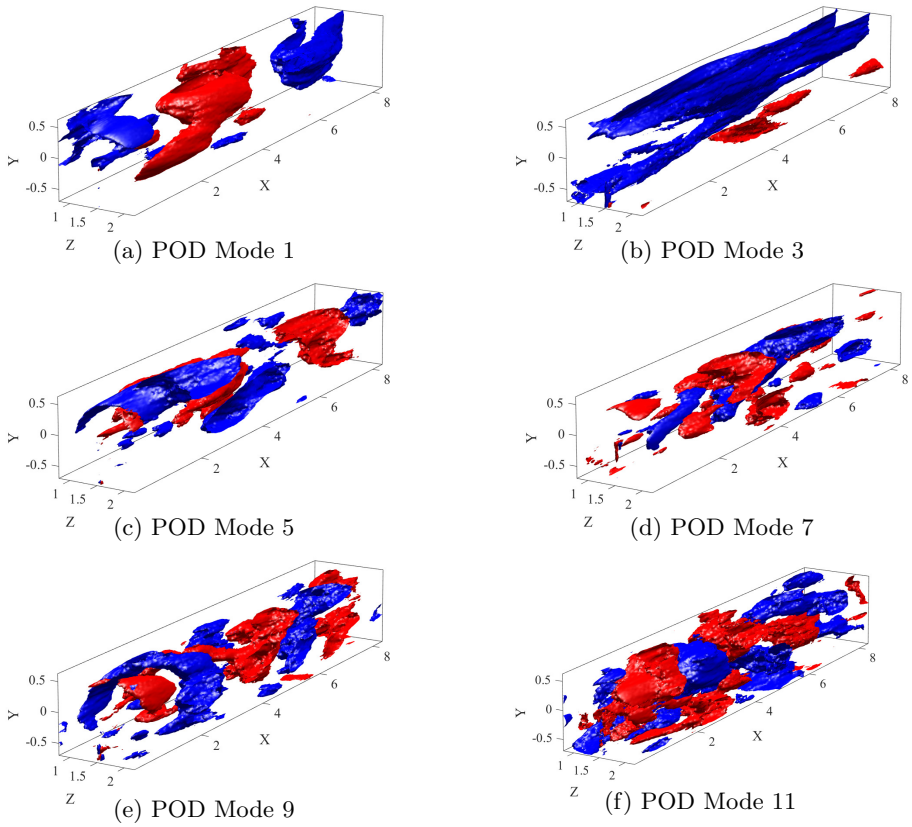

Figure 5: Streamwise velocity iso-surfaces of the most energetic POD modes (red for $u = 0.001$, blue for $u = -0.001$) for the turbulent-inflow case.

structures of rather larger wavelength (more than one diameter long) filling the whole domain.

In order to further analyse these modes, by linking their spatial length scale with their harmonic temporal content, we have performed Fourier transform of the time coefficients $a_k(t)$ associated with the most energetic POD modes. The left (right) column of figure 6 provides results for the laminar- (turbulent-) inflow cases. Concerning the former case, we start noticing that the third mode, associated with the tip vortices, is characterized by a high-frequency content. In particular, its dominant frequency is $f \approx 6.45$, corresponding to $\omega \approx 42$, which is approximately three times the angular frequency of the rotor. Whereas, all the other energetic modes are characterized by lower-frequency oscillations, in the range $f \in [0.44 - 0.73]$ ($\omega \in [2.44 - 4.58]$). We can also notice that some POD modes are also characterised by a secondary, high-frequency peak, not linked to a harmonic of the primary one. This might be expected, since POD does not provide mono-chromatic modes, but energetic coherent structures with multiple temporal and spatial wavenumbers. Table 1 provides the dominant temporal wavenumbers of the six most energetic pairs of the laminar-inflow case, for a direct comparison with the turbulent-inflow case. Concerning the latter case, the right column of figure 6 shows that its most energetic modes are characterized by very low- temporal frequencies (although some weak high-frequency secondary peak can be identified as well). Table 1 shows that in this case the dominant frequencies are rather lower than in the previous , being mostly close to 1 instead of ≈ 3.
Finally, to further characterize the spatial structure of the modes, Fourier transform in the x

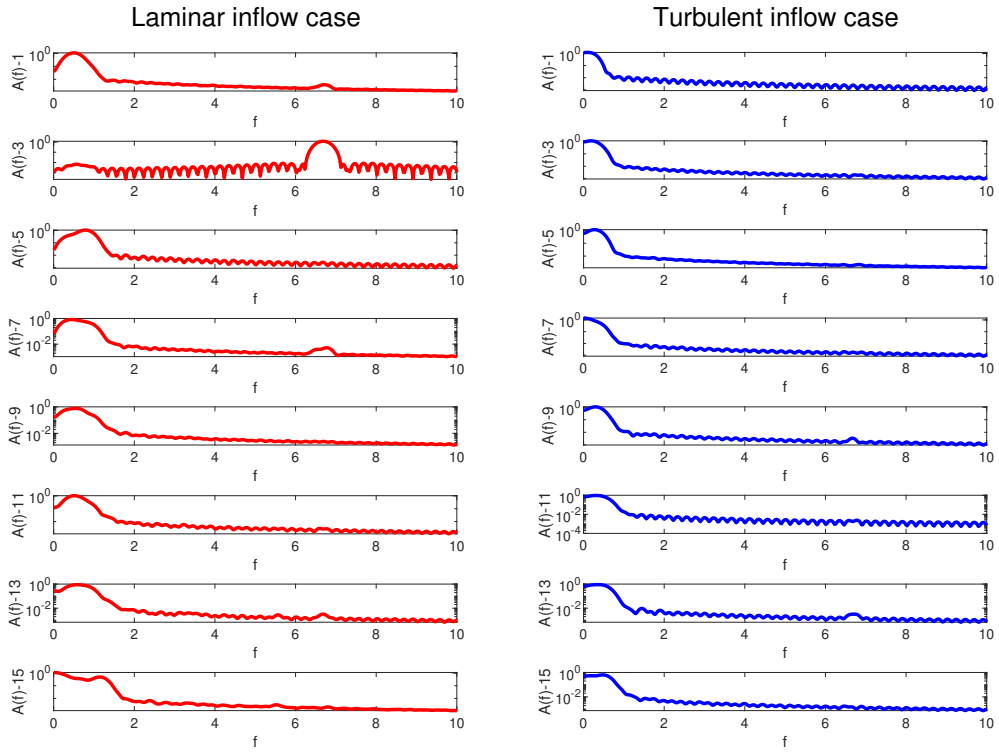

Figure 6: Fourier transform of the time coefficients $a_k(t)$ associated with the most energetic POD modes shown in figure 4 (left column, laminar-inflow case) and 5 (right column, turbulent-inflow case).

	$\Re(\omega)$-POD-lam	$\Re(\omega)$-POD-turb
Pair 1	3.26	0.67
Pair 2	42.0	1.18
Pair 3	4.58	1.68
Pair 4	2.23	0
Pair 5	2.44	1.85
Pair 6	3.76	1.85

Table 1: Main temporal frequency of the first six POD pairs, for the laminar (second column, shown in figure 4) and turbulent inflow (third column, shown in figure 5) cases.

direction is performed for the $y = 0$ plane, as shown in figure 7. The comparison of the dominant spatial wavenumber of the most energetic modes in the two considered cases confirms the fact that the turbulent-inflow case is characterized by modes of much lower spatial and temporal frequency than the laminar-inflow case. In the next subsection, we will investigate how these differences in the structure and frequencial content of the modes affect the wake recovery rate.

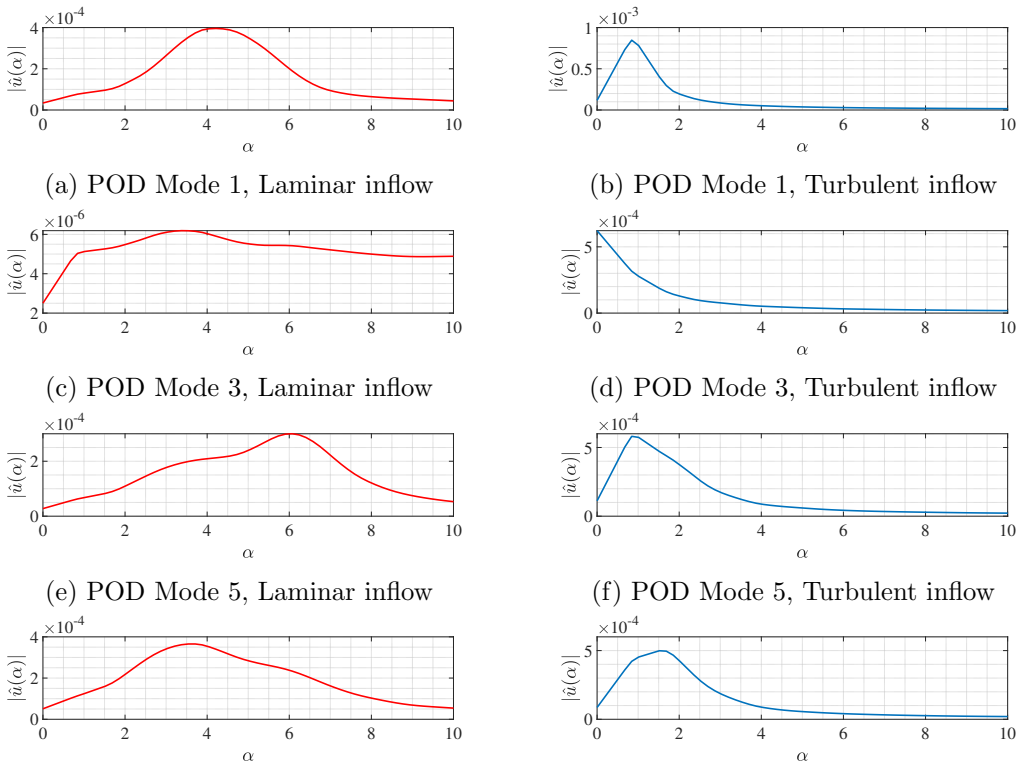

(a) POD Mode 1, Laminar inflow
(b) POD Mode 1, Turbulent inflow
(c) POD Mode 3, Laminar inflow
(d) POD Mode 3, Turbulent inflow
(e) POD Mode 5, Laminar inflow
(f) POD Mode 5, Turbulent inflow
(g) POD Mode 7, Laminar inflow
(h) POD Mode 7, Turbulent inflow

Figure 7: Spatial Fourier spectra versus streamwise wavenumber for the four most energetic POD pairs in the laminar-inflow (left) and the turbulent-inflow (right) cases.

5. Mean kinetic energy entrainment

Recent research [24, 25, 26] suggests that a higher turbulence intensity impinging on a wind turbine increases the wake recovery rate, since the diffusion provided by the turbulent fluctuations improves the transport of mean kinetic energy within the wake. This hypothesis can be assessed for the NREL-5MW wind turbine, by evaluating the contribution of each POD mode to wake recovery. In particular, following Ref. [14], this can be done making use of the the mean kinetic energy (M.K.E.) transport equation:

$$0 = -\bar{u}_j \frac{\partial}{\partial x_j}\left(\frac{1}{2}\bar{u}_i\bar{u}_i\right) - \frac{\partial}{\partial x_i}(\bar{u}_i p) + \bar{u}_i \bar{F}_i + \frac{1}{Re}\nabla^2\left(\frac{1}{2}\bar{u}_i\bar{u}_i\right) - \frac{1}{Re}\frac{\partial \bar{u}_i}{\partial x_j}\frac{\partial \bar{u}_i}{\partial x_j} + \underbrace{-\frac{\partial}{\partial x_j}\left(\bar{u}_i\overline{u_i'u_j'}\right) - \frac{\partial}{\partial x_j}(\bar{u}_i\overline{\tau_{ij}})}_{\text{Turbulent M.K.E. flux}} + \overline{u_i'u_j'}\frac{\partial \bar{u}_i}{\partial x_j} + \overline{\tau_{ij}}\frac{\partial \bar{u}_i}{\partial x_j}, \tag{9}$$

where the Einstein notation of repeated indexes has been used, and $\bar{\cdot}$ denotes long-time average, while primes indicate the fluctuations with respect to the mean. Notice that the turbulent M.K.E. flux is the most important term for wake recovery [35, 14, 36], while the subgrid-scale stresses are supposed to have a negligible contribution to the turbulent M.K.E. flux, at least with respect to the Reynolds stress terms.

Using these hypotheses, the total M.K.E. flux per unit area due to the turbulent fluctuations entering a generic closed surface S can be evaluated by means of the following equation:

$$\mathscr{F}_T = \frac{1}{S}\int_V -\frac{\partial}{\partial x_j}\left(\bar{u}_i\overline{u_i'u_j'}\right)dV, \tag{10}$$

V being the volume enclosed by the surface S. Since the POD modes are orthogonal each other, the Reynolds stress tensor can be decomposed as:

$$\overline{u_i' u_j'} = \overline{\sum_{k=1}^{N}(a_k \phi_i^k) \sum_{l=1}^{N}(a_l \phi_j^l)} = \sum_{k=1}^{N}\sum_{l=1}^{N} \overline{a_k a_l} \phi_i^k \phi_j^l = \sum_{k=1}^{N} \lambda_k \phi_i^k \phi_j^k, \tag{11}$$

which allows to compute the contribution of each POD mode to the turbulent M.K.E. flux as:

$$\mathscr{F}_T^k = \frac{1}{S}\int_V -\frac{\partial}{\partial x_j}\Big(\bar{u}_i \lambda_k \phi_i^k \phi_j^k\Big) dV. \tag{12}$$

We rewrite the last equation as a surface integral as:

$$\mathscr{F}_T^k = \frac{1}{S}\int_S -\bar{u}_i \lambda_k \phi_i^k \phi_j^k dS_j. \tag{13}$$

For evaluating the turbulent M.K.E. flux entering the wake, we consider a cylindrical domain of radius R_c and length L_c centered on the rotor axis. Since we are interested in computing the flux entering the lateral surface of the cylinder, the vector representing the infinitesimal surface element $\boldsymbol{dS}$ is normal to x and can be expressed in Cartesian coordinates as:

$$\boldsymbol{dS} = (0, dc_2, dc_3)\, dx, \tag{14}$$

dc_2 and dc_3 being the components in the vertical and transverse directions of the vector $\boldsymbol{dc}$ normal to the infinitesimal arc of the cylinder circumference C. Thus, we can compute the total flux per unit area of turbulent M.K.E. for each POD mode over the lateral surface of the cylinder as:

$$\mathscr{F}_T^k = \int_{L_c} f_T^k(x) dx, \tag{15}$$

where $f_T^k(x)$ is the local flux, computed for a circumference of radius $R_c = 0.5$ as:

$$f_T^k(x) = -\frac{1}{2\pi R_c L_c}\int_C \bar{u}_i(x) \lambda_k \phi_i^k(x) \phi_j^k(x) dc_j. \tag{16}$$

For each POD mode, the total flux $\mathscr{F}_T^k$ through the surface is computed for different radii in the range $R_c \in [0.35\ 0.62]$.

Figure 8(a) shows that, for the laminar-inflow case, the most energetic POD pair found in the near-wake region (red line), which is directly related to the tip and root vortices, provides mostly negative M.K.E. local flux at $R_c = 0.5$. Whereas, all the others intermediate-scale modes induce mostly a positive flux, although localized in the far-wake region ($x > 8$). As shown in figure 8(b), the total flux of the tip-vortex related POD mode is negative for all $R_c < 0.55$, and almost zero for $R_c \geq 0.55$. Whereas, the other POD modes provide a positive contribution to the turbulent M.K.E. of the wake. Increasing the cylinder radius to $R_c > 0.5$, the total flux decreases but does not changes sign. Thus, as already discussed in Ref. [18, 17] (although for much smaller turbines and Reynolds numbers), the tip vortices appear to contribute to the sustainment of the wake, rather than to its recovery.

We now compare these results with those of the turbulent-inflow case, provided in Figure 9. The local flux for $R_c = 0.5$, shown in figure Figure 9(a), indicates that all the low-frequency most energetic POD modes discussed before, provide positive M.K.E. local flux. The local flux peaks at $x \approx 6$ for almost all most energetic modes, and slowly decreases towards the far wake. The total flux for different values of R_c and for the six most energetic pairs of modes, is provided

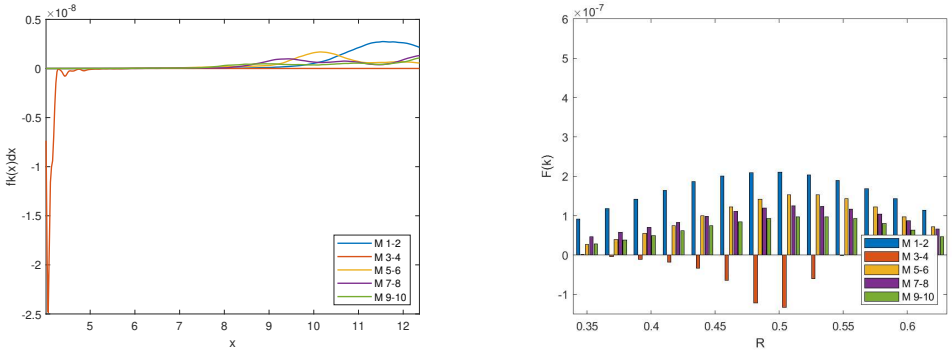

(a) (b)

Figure 8: M.K.E. entrainment for the laminar-inflow case: local (a) and total (b) fluxes.

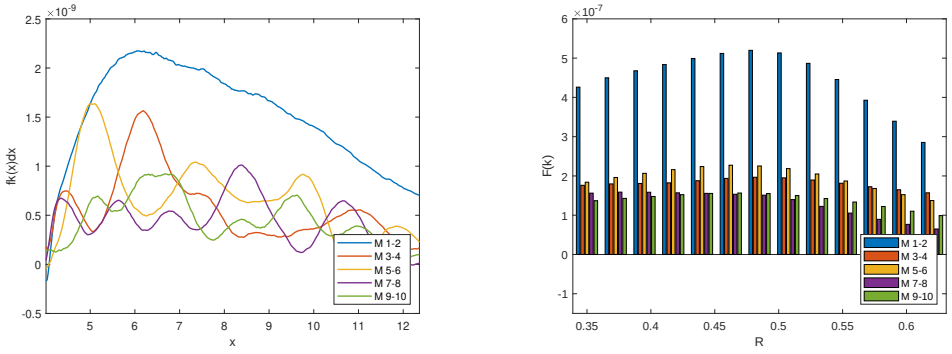

(a) (b)

Figure 9: M.K.E. entrainment for the turbulent-inflow case: local (a) and total (b) fluxes.

in Figure 9(b). All the modes provide a positive contribution to the M.K.E. entrainment, especially the most energetic one, whose total flux is more than double that of its laminar-inflow counterpart. These results clearly show that inflow turbulence has a strong impact on M.K.E. entrainment, and thus it cannot be neglected for numerically evaluating the wake recovery rate of wind turbines. Moreover, we have found that long wavelength, low-frequency coherent structures appear beneficial for accelerating wake recovery.

6. Conclusion

In wind farms, the turbines are aerodynamically coupled to each-other through the presence of their wakes, since depending on their relative position, waked turbines might produce considerably less power. Thus, an accurate prediction of the wake recovery rate of the upstream turbines is paramount for evaluating the power production of wind farms and designing the turbine's placement. In this context, the present work aims at investigating the effect of inflow turbulence on the wake recovery of the NREL-5MW reference wind turbine, by means of Proper Orthogonal Decomposition, which allows one to recover the most energetic coherent structures within the wake.

Towards this goal, the wake produced by a utility-scale wind turbine is numerically reproduced by means of Large Eddy Simulations. The considered turbine is the NREL-5MW at tip-speed ratio $\lambda = 7$ and a diameter-based Reynolds number of the order 10^8. The forces exerted by the

blades are modeled using the Actuator Line Method, whereas tower and nacelle are modeled with the Immersed Boundary Method. Two cases are considered: in the former, the turbine is impinged by a laminar uniform inflow, while in the latter a turbulent inflow is considered. The snapshots extracted from the numerical code are used as a dataset for POD, which allows to identify the most energetic coherent structures within the flow. The POD modes obtained in the laminar-inflow and in the turbulent-inflow cases are compared, and some differences emerge, which can be of great importance for the formulation of a reduced-order model. In the laminar-case, a high-frequency mode directly related to the tip vortices is found, together with modes with an intermediate (less then one diameter) length scale, located in the far-wake region. Whereas, in the presence of inflow turbulence, the most energetic modes are all characterized by large-scale low-frequency structures filling the whole domain.

The contribution of each of these modes to the entrainment of turbulent kinetic energy within the wake is evaluated by computing its flux on a closed surface enclosing the wake of the wind turbine. It is found that the POD modes related to the tip and root vortices, which are highly energetic in the laminar-inflow case, contribute negatively to the wake recovery. As discussed in Ref. [18] for a different wind turbine, they appear to sustain the velocity gradient of the wake. Whereas, when the turbine is impinged by a turbulent inflow, all the energetic modes contribute positively to wake recovery. These results clearly show that inflow turbulence has a strong impact on the entrainment of turbulent kinetic energy within the wake. Thus, turbulence of the inflow cannot be neglected for accurately estimating the wake recovery rate of wind turbines. Moreover, our results indicate that long wavelength, low-frequency coherent structures are beneficial for accelerating wake recovery. This can be of interest for setting up control or design methods for ensuring a rapid recovery of the turbine's wakes.

[1] European Commission 2021 National energy and climate plans 2021-2030 Tech. rep. European Commission
[2] REPN 2019 Renewables 2019 global status report Tech. rep. Renewable Energy Policy Network for the 21st Century
[3] IRENA 2019 Smart electrification with renewables: Driving the transformation of energy services Tech. rep. International Renewable Energy Agency, Abu Dhabi
[4] IEA 2019 Renewable 2019. market analysis and forecast from 2019 to 2024. Tech. rep. International Energy Agency
[5] Stevens R J and Meneveau C 2017 *Annual review of fluid mechanics* **49**
[6] Porté-Agel F, Bastankhah M and Shamsoddin S 2019 *Boundary-Layer Meteorology* 1–59
[7] Goit J P and Meyers J 2015 *Journal of Fluid Mechanics* **768** 5 – 50
[8] Munters W and Meyers J 2018 *Journal of Physics: Conference Series* **1037** 032015
[9] Bernardoni F, Ciri U, Rotea M A and Leonardi S 2021 *Journal of Renewable and Sustainable Energy* **13** 043301
[10] Cossu C 2021 *Wind Energy* **24** 345–356
[11] Sirovich L 1987 *Quarterly of applied mathematics* **45** 561–590
[12] Berkooz G, Holmes P and Lumley J L 1993 *Annual review of fluid mechanics* **25** 539–575
[13] Schmid P J 2010 *J. Fluid Mech.* **656** 5–28
[14] VerHulst C and Meneveau C 2014 *Physics of Fluids* **26** 025113
[15] Hamilton N, Tutkun M and Cal R B 2015 *Wind Energy* **18** 297–315
[16] De Cillis G, Cherubini S, Semeraro O, Leonardi S and De Palma P 2020 *Journal of Physics: Conference Series* **1618** 062016
[17] De Cillis G, Cherubini S, Semeraro O, Leonardi S and De Palma P 2021 *Wind. Energy* **24** 609–633
[18] Lignarolo L, Ragni D, Scarano F, Ferreira C S and Van Bussel G 2015 *Journal of Fluid Mechanics* **781** 467–493
[19] Medici D 2005 *Experimental studies of wind turbine wakes: power optimisation and meandering* Ph.D. thesis KTH
[20] Wu Y T and Porté-Agel F 2013 *Boundary-layer meteorology* **146** 181–205
[21] Chu C R and Chiang P H 2014 *Journal of Wind Engineering and Industrial Aerodynamics* **124** 82–89
[22] Chamorro L P, Arndt R and Sotiropoulos F 2011 *Boundary-layer meteorology* **141** 349–367
[23] De Cillis G, Cherubini S, Semeraro O, Leonardi S and De Palma P 2022 *Renewable Energy* **183** 601–616 ISSN 0960-1481
[24] Hansen K S, Barthelmie R J, Jensen L E and Sommer A 2012 *Wind Energy* **15** 183–196

[25] Wu Y T and Porté-Agel F 2012 *energies* **5** 5340–5362
[26] Talavera M and Shu F 2017 *Renewable Energy* **109** 363–371
[27] Iungo G V, Wu Y T and Porté-Agel F 2013 *Journal of Atmospheric and Oceanic Technology* **30** 274–287
[28] Aitken M L and Lundquist J K 2014 *Journal of Atmospheric and Oceanic Technology* **31** 1529–1539
[29] Orlandi P 2000 *Fluid flow phenomena: a numerical toolkit* (*Fluid Mechanics and Its Applications* vol 55) (Springer Netherlands)
[30] Sørensen J N and Shen W Z 1999 Computation of wind turbine wakes using combined navier-stokes/actuator-line methodology *1999 European Wind Energy Conference and Exhibition* pp 156–159
[31] Orlandi P and Leonardi S 2006 *Journal of Turbulence* N73
[32] De Cillis G, Cherubini S, Semeraro O, Leonardi S and De Palma P 2022 *Renewable Energy* **181** 765–785 ISSN 0960-1481
[33] Orlanski I 1976 *J. Comput. Phys.* **21** 251–269
[34] Cheng W C and Porté-Agel F 2015 *Boundary-Layer Meteorology* **155** 249–270
[35] Santoni C, Carrasquillo K, Arenas-Navarro I and Leonardi S 2017 *Wind Energy* **20** 1927–1939
[36] Cal R B, Lebrón J, Castillo L, Kang H S and Meneveau C 2010 *Journal of Renewable and Sustainable Energy* **2** 013106